Perturbational profiling of nanomaterial biologic activity

Stanley Y. Shaw*†‡, Elizabeth C. Westly*, Mikael J. Pittet†§, Aravind Subramanian*, Stuart L. Schreiber*¶‖, and Ralph Weissleder†§‖

*Broad Institute of Harvard and MIT, 7 Cambridge Center, Cambridge, MA 02142; †Center for Systems Biology, ‡Cardiovascular Research Center, and §Center for Molecular Imaging Research, Massachusetts General Hospital and Harvard Medical School, 185 Cambridge Street, Boston, MA 02114; and ¶Howard Hughes Medical Institute and Department of Chemistry and Chemical Biology, Harvard University, 12 Oxford Street, Cambridge, MA 02138

Contributed by Stuart L. Schreiber, March 21, 2008 (sent for review February 24, 2008)

Our understanding of the biologic effects (including toxicity) of nanomaterials is incomplete. *In vivo* animal studies remain the gold standard; however, widespread testing remains impractical, and the development of *in vitro* assays that correlate with *in vivo* activity has proven challenging. Here, we demonstrate the feasibility of analyzing *in vitro* nanomaterial activity in a generalizable, systematic fashion. We assessed nanoparticle effects in a multidimensional manner, using multiple cell types and multiple assays that reflect different aspects of cellular physiology. Hierarchical clustering of these data identifies nanomaterials with similar patterns of biologic activity across a broad sampling of cellular contexts, as opposed to extrapolating from results of a single *in vitro* assay. We show that this approach yields robust and detailed structure–activity relationships. Furthermore, a subset of nanoparticles were tested in mice, and nanoparticles with similar activity profiles *in vitro* exert similar effects on monocyte number *in vivo*. These data suggest a strategy of multidimensional characterization of nanomaterials *in vitro* that can inform the design of novel nanomaterials and guide studies of *in vivo* activity.

cluster analysis | molecular imaging | nanoparticles

The expanding use of nanomaterials has spurred interest in defining their biologic effects (1). Traditionally, the *in vivo* biologic and toxic effects of nanomaterials have been revealed via animal studies. For instance, single-wall carbon nanotubes cause pulmonary granulomas upon intratracheal instillation in rats and mice (2, 3). Although extremely informative, animal studies are costly and labor-intensive and thus ill-suited to systematically explore the sheer number of potential nanomaterial variables that can influence *in vivo* activity (including size, core material, coating, surface functionalization, and nanoscale and physicochemical properties). *In vitro* assays in cultured cells, although unlikely to substitute for animal studies, could help dissect structure–activity relationships and suggest nanomaterials likely to have favorable *in vivo* activity (4).

Although numerous studies have used cultured cell models to examine nanomaterial toxicity, extrapolating from *in vitro* to *in vivo* activity remains challenging. In addition to the complexities of *in vivo* pharmacokinetics and bioavailability, cellular phenotypes (such as the repertoire of expressed proteins) can change significantly during *in vitro* cell culture (5); furthermore, nanomaterials may show significant *in vitro* toxicity in one cell-based assay but not others (6). Most commonly, these *in vitro* efforts have evaluated nanomaterials based on a single cell line and by using a limited number of phenotypes (often a single assay). This makes any conclusions critically dependent on the particular choice of cell model and assay and offers a relatively narrow view of the potentially pleiotropic ways in which a nanomaterial can modulate living systems.

We sought to develop a generalizable systematic approach that would provide a more comprehensive view of the biological effects induced by a nanomaterial and improve correlations with *in vivo* observations. In this approach, the biologic activity of a nanomaterial is assessed by multiple physiologic cell-based assays, in multiple cell types, and at multiple doses. Each nanomaterial (NM) can then be characterized by a profile P(NM) = $\{Z_{ijk}\}$, in which each feature is the normalized assay result Z_{ijk} that results when the nanomaterial is added at dose i to cell type j, and its effect is measured using assay k. Each profile is thus composed of $(i \times j \times k)$ features. This profile samples a much broader swath of biology than is accessible by characterizing a material in a single cell type and using a single phenotype. Clustering methods can then classify nanomaterials into groups based on similarities in their profiles (i.e., based on similarities in their patterns of biologic effects in many different cellular contexts). This approach is analogous to the use of gene expression data to discover novel classifications among tumor samples (7) but with cell-based physiologic measurements in place of levels of gene expression. Furthermore, the use of multiple cell lines (vs. a single cell line) has yielded novel insights into mechanisms of anticancer drug action and resistance (8, 9).

Because the unit of comparison among nanomaterials is a profile that reflects multiple cellular assays and cell types, the goal of this analysis is not to extrapolate from the results of a particular *in vitro* assay to a specific *in vivo* phenotype. Rather, the goal is to analyze the broad patterns of activity of the nanomaterials relative to one another, and identify nanomaterials that cause similar biologic effects; one can then test whether nanomaterials with similar activity *in vitro* also behave similarly *in vivo*.

As a proof-of-concept for this approach, we evaluated 50 different nanomaterials at four different doses in four cell types, using four physiologic assays. We demonstrate that this high-dimensionality analysis results in different relationships among nanoparticles compared with those ascertained by more limited data subsets. The data also reveal how alterations in nanomaterial composition (e.g., core composition, coating, and surface functionalization) can modulate biologic activity. Equally important, we further evaluate three commonly used nanoparticles *in vivo* (by measuring changes in monocyte number after i.v. injection), and demonstrate that their relative *in vivo* phenotypes correlate with their *in vitro* profiles.

Results

Nanomaterials and Experimental Conditions. The 50 nanomaterials analyzed possess varying core compositions, coatings, and surface attachments. We focused primarily on nanoparticles used for molecular imaging and nanosensing because of their potential widespread use in medical applications (10) and because prepara-

Author contributions: S.Y.S., M.J.P., S.L.S., and R.W. designed research; S.Y.S., E.C.W., and M.J.P. performed research; S.Y.S., M.J.P., and A.S. analyzed data; and S.Y.S., M.J.P., S.L.S., and R.W. wrote the paper.

The authors declare no conflict of interest.

‖To whom correspondence may be addressed. E-mail: stuart_schreiber@harvard.edu or rweissleder@mgh.harvard.edu.

This article contains supporting information online at www.pnas.org/cgi/content/full/0802878105/DCSupplemental.

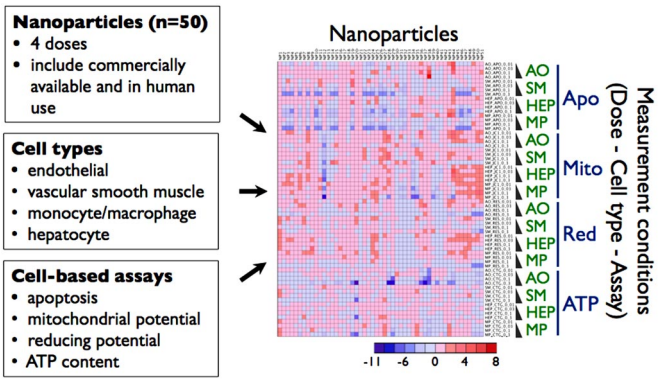

Fig. 1. Determining biologic activity of nanoparticles. The heat map displays *Z* scores for each nanoparticle (in columns) under 64 different conditions (in rows, all combinations of four doses × four cell types × four assays). Wedge shapes indicate increasing nanoparticle dose. AO, aorta endothelial cell; SM, vascular smooth muscle; HEP, hepatocyte; MP, monocyte/macrophage; Apo, apoptosis assay; Mito, mitochondrial potential assay; Red, reducing equivalents assay; ATP, ATP content assay.

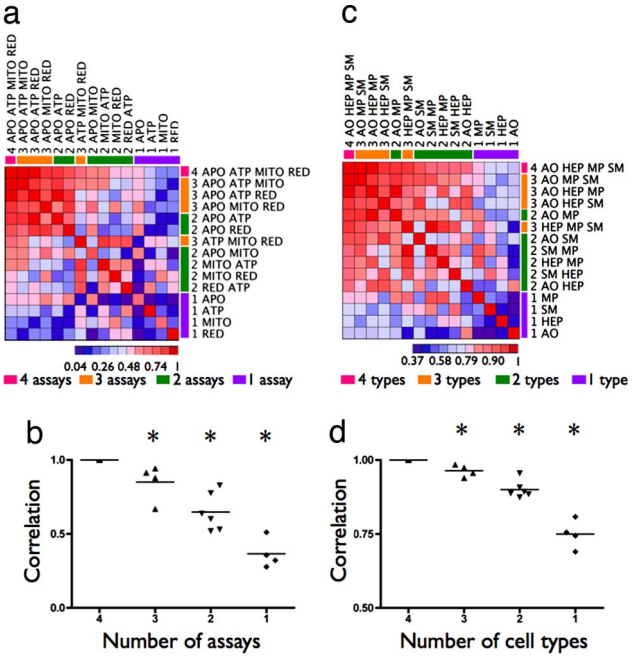

Fig. 2. Comparison of nanoparticle activity profiles in the complete dataset vs. data subsets. (*a*) Correlation between complete dataset and subsets that include varying numbers (and combinations) of assays. Columns and rows are named according to the number (1, 2, 3, or 4) and names of the assays included in the subset. (*b*) Scatter plots of Pearson correlations between the complete dataset and subsets that include one, two, or three assays. Each point represents the correlation value between the complete dataset and a specific combination of assays. (*c*) Correlation between complete dataset and subsets that include varying numbers (and combinations) of cell types. (*d*) Scatter plot of Pearson correlations between the complete dataset and subsets that include one, two, or three cell types. Assay and cell type abbreviations are the same as in Fig. 1.

tions approved for human use can be used as reference materials. The nanoparticles (NP) belong to five categories or platforms: (*i*) cross-linked iron oxide (CLIO)-based, consisting of a superparamagnetic iron oxide core and a covalently cross-linked dextran coating (NP1-NP23) (11); (*ii*) pseudocaged nanoparticle (PNP)-based, containing either superparamagnetic or para/dia-magnetic iron oxide cores and a variety of polymer coatings (NP26-NP44); (*iii*) monocrystalline iron oxide nanoparticle (MION)-based, consisting of a superparamagnetic iron oxide core and an incomplete non-cross-linked dextran coating (NP45-NP48) (12); (*iv*) quantum dot-based, with a CdSe core, a ZnS shell, and a polymer coating (NP49-NP51) (13); and (*v*) the following iron-based nanoparticles approved for human use: Feridex IV (approved for *in vivo* imaging, with a polydisperse superparamagnetic core and incomplete dextran coating) (NP24) and Ferrum Hausmann (approved for iron supplementation, with a Fe(III) $(OH)_3$ core and sucrose coating) (NP25) [see supporting information (SI) Table S1 for details].

We chose to evaluate each nanomaterial under all possible combinations of the following conditions (Fig. 1): (*i*) 4 concentrations over a 30-fold range (0.01 to 0.3 mg/ml Fe for iron-based nanoparticles; 3–100 nM for quantum dots) that span the range typically encountered in *in vivo* applications; (*ii*) the following four cell types, selected for this experiment to reflect a range of tissues relevant for evaluation of the intravascularly administered agents: vascular cells (endothelial and smooth muscle cells), monocytes [which take up many nanoparticle imaging agents (14)], and hepatocytes (because of the importance of hepatotoxicity in evaluating novel agents); and (*iii*) the following four cell-based assays that are widely used, amenable to high-throughput data collection, reflect complementary aspects of cellular viability and physiology, and have been used to assess nanomaterial toxicity: ATP content (15), reducing equivalents (16), caspase-mediated apoptosis (15), and mitochondrial membrane potential (17).

The entire dataset comprises measurements from ≈24,000 wells, including control and replicate wells. Each measurement was made in quadruplicate; assay values are expressed in units of standard deviations of the distribution obtained when cells are treated with PBS alone (*Z* score). The *Z* scores in the dataset (depicted in the heat map in Fig. 1) skew slightly toward negative values, with mean = −0.49, standard deviation = 1.4, and 95% confidence interval = −3.2–2.2 (Fig. S1). In subsequent analyses, each nanoparticle is represented by a profile of 64 features consisting of the assay *Z* scores for all possible combinations of dose, cell type and assay as described in the Introduction (and corresponding to individual columns in the heat map in Fig. 1).

Multiple Assays and Cell Types Enrich Nanomaterial Biologic Activity Profiles. The activity profiles for the vast majority of nanoparticles reveal a heterogeneous range of responses (Fig. 1). This suggests that data from a single cell type or assay may not reflect all of the biologic information captured by the full activity profile.

To quantitatively test this hypothesis, we asked whether the correlation between the activity profiles of any two nanoparticles changes significantly when we vary the number of assays or cell types in the analysis. We calculated all possible pairwise correlations between nanoparticles, using the full complement of 64 features per particle (i.e., all doses, cell types, and assays in the complete dataset). We then recalculated these pairwise correlations for all possible subsets of the dataset (e.g., including only data from one, two, or three assays, or one, two, or three cell types). Finally, we assessed how correlations between nanoparticles in a given data subset correlated with those in the complete dataset.

In general, the degree of correlation with the complete dataset improves progressively as one increases the number of assays in the analysis from 1 to 4 (Fig. 2*a*). Data subsets that use one, two, or three assays show a progressive and statistically significant increase in correlation with the complete dataset ($P = 0.0005$ for ANOVA; $P = 5.5 \times 10^{-4}, 5.5 \times 10^{-4}$, and 0.048 for subsets including one, two, or three assays, respectively) (Fig. 2*b*). Thus, the relationships between nanoparticles change significantly as one moves from one assay to four assays. Analogous results ensue when the number of cell types included in the analysis is varied (Fig. 2 *c* and *d*; $P < 0.0001$

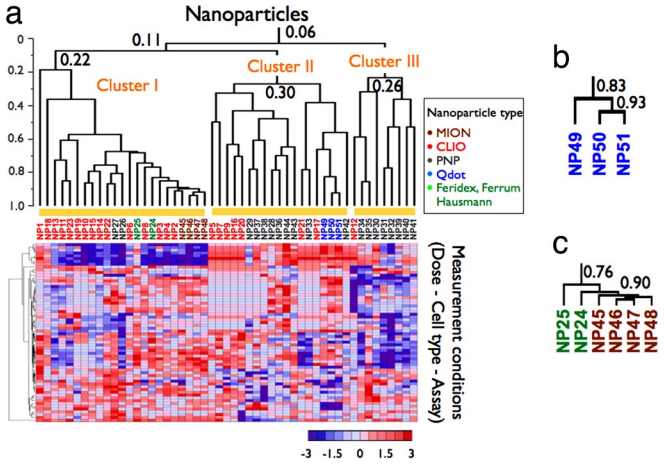

Fig. 3. Hierarchical clustering of nanoparticles based on activity profiles. (*a*) Heat map depicting hierarchical clustering of nanoparticle biological activity in the entire dataset. *Z* scores are depicted in each cell; nanoparticle labels are color-coded to reflect their underlying platform (Table S1). Numbers adjacent to nodes in the dendrogram indicate the correlation value for that node, with the correlation scale along the left. (*b*) Dendrogram of a subcluster containing all three quantum dots (NP 49–NP51) (see Table 1 and Table S1). (*c*) Dendrogram of hierarchical clustering of two nanoparticles in our dataset approved for human use (NP24, Feridex IV, and NP25, Ferrum Hausmann) and four MION-based nanoparticles (NP45–NP48) (see Table 1 and Table S1).

for ANOVA; $P = 9.5 \times 10^{-4}$, 2.0×10^{-4}, and 0.018 for subsets including one, two, or three cell lines, respectively). Together, these results argue that our ability to detect relationships among nanoparticles (i.e., similarity or differences in their biologic effects) is significantly enhanced by evaluating them in multiple different cellular assays and cell types. Interestingly, at a given number of assays, those combinations that include the apoptosis assay are ranked the highest (i.e., are the most similar to the complete dataset) (Fig. 2*a*), suggesting that it may contribute more to the nanoparticle correlations than the other assays.

Hierarchical Clustering and Class Prediction of Nanoparticles Based on Biological Activity. We performed unsupervised hierarchical and consensus clustering to group the nanoparticles based on their activity profiles and investigate how nanomaterial composition influences biologic activity. Consensus clustering increases the robustness of hierarchical clustering by iteratively repeating the hierarchical clustering algorithm, each time subsampling the data; the output of consensus clustering is the fraction of clustering runs in which any two samples (nanoparticles) cluster together (18). The greater the coclustering frequency, the more robust the putative clusters are, and the more likely it is that the clusters reflect some true underlying structure within the dataset.

Hierarchical clustering analysis (using the Pearson correlation) divides the 50 nanoparticles into three main groups or clusters (Fig. 3*a*). Overall, the nanoparticles show very divergent activity profiles. For instance, the correlation value for the top node in the cluster diagram is 0.06; the correlation for the node joining cluster III with the cluster I/cluster II branch is 0.11; in comparison, the top nodes defining clusters I, II, and III have correlation values ranging from 0.22 to 0.30. Within each cluster, subsets of related nanoparticles have highly correlated profiles. For instance, the correlation between NP50 and NP51 (cluster II), replicates of the same carboxyl-modified quantum dot, is 0.93; furthermore, all three quantum dot samples (NP 49–51) cluster closely together, subtended by a node with a correlation of 0.83 (Fig. 3 *a* and *b* and Table S1). Similarly, cluster I contains a highly correlated cluster (correlation value = 0.76) that contains the two nanoparticles approved for human use (NP24, Feridex, and NP25, Ferrum Hausmann), and a series of nanoparticles (NP45–NP48) based on a platform that has completed phase III clinical trials (Combidex or Ferumoxtran-10) (Fig. 3 *a* and *c* and Table S1). In addition to these functionally meaningful groupings, each cluster also contains more than one nanoparticle platform and a variety of surface modifications. The heterogeneity within each cluster suggests that biologic activity arises from the combined effects of many aspects of nanoparticle composition and is therefore difficult to predict *a priori*. Taken together, these data suggest that the nanoparticle collection causes a diverse range of biologic responses but that our methodology yields high correlation values for nanoparticles that share physical, chemical, or biological properties.

We tested whether the nanoparticles' activity profiles encode sufficient information to correctly assign them to the correct cluster ("class prediction"). We selected clusters I and II for this test, because they are the largest clusters of relatively symmetric size (24 and 20 members, respectively); this also constituted the most demanding test, because clusters I and II are the most highly correlated pair among the three clusters. We first randomly divided the nanoparticles into a training and testing set (each containing 22 nanoparticles, stratified by membership in cluster I vs. cluster II). We then analyzed the training set to select features that best discriminate between cluster I vs. cluster II ("class predictor") and applied the class predictor to assign nanoparticles in the testing set to either cluster I or cluster II. Using three different class prediction algorithms [classification and regression trees, k-nearest-neighbors, and weighted voting], we were able to predict membership in cluster I vs. II with impressive accuracies of 20/22 (0.91), 18/22 (0.82), and 19/22 (0.86), respectively. Of note, when we included zeta potentials (a widely used measure of the electrostatic potential at the nanoparticle surface double layer) as a feature for each nanoparticle, the zeta potential did not distinguish between cluster I vs. II compared with other features (Fig. S2 *a* and *b*).

Structure–Activity Relationships Revealed Through Clustering Analysis. The large number of nanoparticles in our dataset allows us to study how specific changes in nanoparticle composition affect their biologic activity. For instance, particles NP26, NP27, NP31, and NP32 represent all four possible combinations of two cores (superparamagnetic vs. paramagnetic iron oxide), and two surface modifications (ethylene diamine vs. carboxylic acid; see Table 1 and Table S1). In the original dataset, NP26 and NP27 fall in cluster I, and NP31 and NP32 fall in cluster III (Fig. 3*a*). If these four particles are reanalyzed together, consensus clustering indicates that NP26 and NP27 consistently cluster together (coclustering frequency = 1) despite their very different surface modifications (e.g., a carboxylic acid vs. the relatively basic ethylene diamine), and that NP31 and NP32 similarly cluster together (coclustering frequency = 1) (Fig. 4*a*); similar conclusions are reached by conventional hierarchical clustering of these four nanoparticles (Fig. S3*a*). These data suggest that, at least for this series of nanoparticles, the core composition can exert a strong and somewhat unanticipated influence on biologic activity.

We extended this analysis to compare eight nanoparticles conjugated to a series of basic peptides [protamine, poly-L-arginine or poly-D-arginine); they also contain different carbohydrate coatings, and either Fe_3O_4 or Fe_2O_3 cores (Table 1). [Nanoparticles bearing basic peptides on their surface can enter a wide variety of cell types and thus serve as universal cell trackers *in vivo* (19).] In the original dataset, the eight nanoparticles are distributed across clusters I, II, and III (Fig. 3*a*). Reanalysis classifies these particles into four groups (Fig. 4*b* and Fig. S3*b*), determined to a significant extent by their surface modifications. Thus, the protamine-conjugated nanoparticles (NP11, NP19, NP23, NP29, and NP38) make up two clusters, largely corresponding to the underlying CLIO vs. PNP platforms (Table 1 and Table S1). The two poly-L-arginine-modified nanoparticles (NP30, NP39) comprise a third group, and the poly-D-arginine-modified nanoparticle (NP42) is a singleton.

Table 1. Brief summary of core and surface modifications for nanoparticles discussed in Figs. 4–6

Particle	Type	Core	Surface	Fig.
NP26	PNP	Fe_3O_4	-COOH	4*a*
NP27	PNP	Fe_3O_4	ethylene diamine	4*a*
NP31	PNP	Fe_2O_3	-COOH	4*a*
NP32	PNP	Fe_2O_3	ethylene diamine	4*a*
NP23	CLIO	Fe_3O_4	VT680, protamine	4*b*
NP11	CLIO	Fe_3O_4	Cy5.5, protamine	4*b*
NP19	CLIO	Fe_3O_4	rhodamine, protamine	4*b*
NP29	PNP	Fe_3O_4	rhodamine, protamine	4*b*
NP38	PNP	Fe_2O_3	rhodamine, protamine	4*b*
NP39	PNP	Fe_2O_3	(L)-arg_7-COOH	4*b*
NP30	PNP	Fe_3O_4	(L)-arg_8-COOH	4*b*
NP42	PNP	Fe_2O_3	(D)-arg_7-COOH	4*b*
NP24	Feridex	Fe_3O_4 (polydisperse)	incomplete dextran	5 and 6
NP3	CLIO	Fe_3O_4 (monodisperse)	complete dextran, -NH_2	5 and 6
NP49	Qdot	CdSe	PEG, -NH_2	5 and 6

Full details may be found in Table S1. "Type" refers to the nanoparticle classifications used in Fig. 3 and the main text.

Note that our analysis clearly separates poly-D- vs. the diastereomeric poly-L-arginine-modified nanoparticles (Fig. 4*b* and Fig. S3*b*), demonstrating the high sensitivity with which we can detect the biologic consequences of subtle surface modifications.

***In Vitro* Relationships Among Nanoparticles Correlate with *in Vivo* Activity.** We hypothesize that nanomaterials that cluster close together in our *in vitro* analysis should also have similar *in vivo* activity; conversely, nanomaterials that cluster into different classes should have disparate *in vivo* activities. We selected three commonly used nanoparticles from our *in vitro* experiments to test these hypotheses in a murine model: (*i*) Feridex IV (NP24), which is FDA-approved as an intravascularly-administered imaging agent and has shown minimal *in vivo* toxicity in rats (20) or humans (21); (*ii*) CLIO-NH_2 (NP3); and (*iii*) Qdot-NH_2-PEG (NP49). Each of these nanoparticles differs in their core composition, coating, and surface functionalization (Table 1 and Table S1). Hierarchical clustering analysis of our *in vitro* data places Feridex IV (NP24) and CLIO-NH_2 (NP3) very close to each other in the same group (Fig. 3*a* and Fig. S3*c*), and they cause very similar assay measurements across all conditions tested (Fig. 5*a*). In contrast, Qdot-NH_2-PEG (NP49) clusters in a distinct group from Feridex IV (NP24) and CLIO-NH_2 (NP3) (Fig. 3*a* and Fig. S3*c*) and shows a distinct assay response profile. In particular, the apoptosis and reducing equivalent assays reveal marked differences in effects induced by Qdot-NH_2-PEG (NP49) vs. either Feridex IV (NP24) or CLIO-NH_2 (NP3) (Fig. 5*b*). (Conversely, the ATP and mitochondrial potential assays fail to distinguish Qdot-NH_2-PEG (NP49) from the other two nanoparticles, illustrating how a wider variety of assays can reveal differences in activity that might otherwise remain undetected.)

All three of these agents are widely used *in vivo* in animal models (and, in the case of Feridex IV, in humans) without obvious evidence of gross end-organ toxicity, suggesting that our *in vitro* clustering analysis reflects a relatively subtle phenotypic distinction between Feridex IV and CLIO-NH_2 in one class and Qdot-NH_2-PEG in another. We chose to examine the *in vivo* effects of these nanoparticles on the monocyte population after a brief exposure for a number of reasons: (*i*) alterations in leukocyte subsets, including increased monocyte fraction, can be a sign of proinflammatory or other toxic exposures (22, 23), (*ii*) monocytes are phagocytic, and take up certain nanoparticles more than many other cell types (14), and (*iii*) nanomaterials have been shown to cause pleiotropic effects on immune cells that are very sensitive to the materials' composition and surface (24).

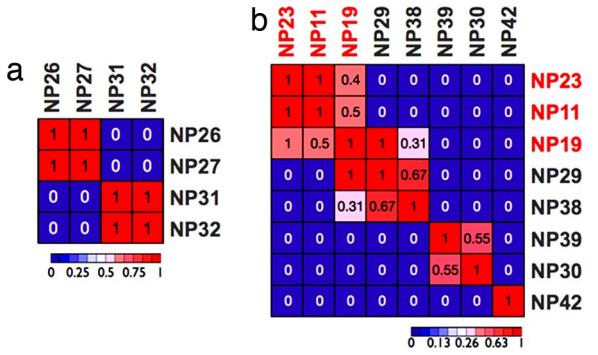

Fig. 4. Structure–activity relationships based on activity profiles. (*a*) Heat map showing results of consensus clustering for NP26, NP27, NP31, and NP32 (Table 1). The color of each cell and the number within each cell reflect the fraction of iterative clustering runs in which two particles cluster together. (*b*) Heat map showing results of consensus clustering for eight nanoparticles that bear different basic peptides on their surface (Table 1).

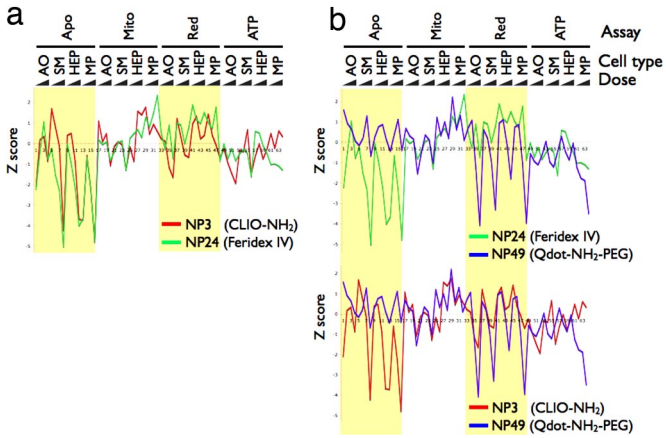

Fig. 5. *In vitro* activity profiles for three commonly used nanoparticles (CLIO-NH_2, Feridex IV, and Qdot-NH_2-PEG) across all experimental conditions (combinations of dose, cell type, and assay). (*a*) *Z* score profile for CLIO-NH_2 and Feridex IV, showing similar *Z* scores across all conditions. (*b*) *Z* score profiles for Feridex IV vs. Qdot-NH_2-PEG (*Upper*) and CLIO-NH_2 vs. Qdot-NH_2-PEG (*Lower*). Divergent *Z* scores between nanoparticles are observed only with the apoptosis and reducing equivalents assays (orange).

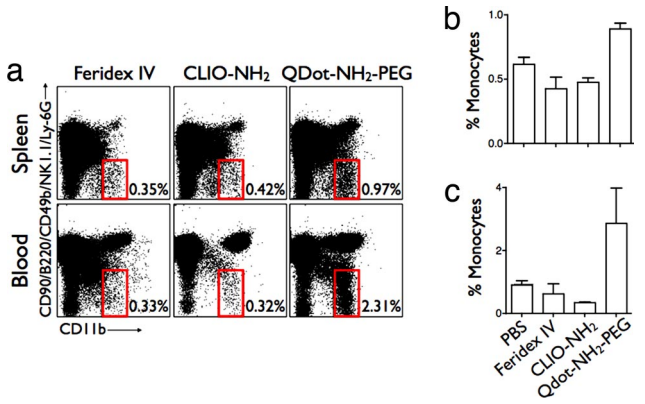

Fig. 6. Effect of intravenously administered nanoparticles on monocyte fractions *in vivo*. (*a*) FACS analysis on representative individual spleen or blood samples after nanoparticle treatment. The fraction of cells that are monocytes (defined as $CD11b^{hi}$ [CD90/B220/CD49b/NK1.1/Ly-6G)^{lo} cells] is indicated. (*b*) Monocyte fractions observed in the spleen after treatment with nanoparticles. (*c*) Monocyte fractions observed in peripheral blood. Values shown are the mean and standard deviation from measurements on three mice.

We quantitated blood and splenic monocytes by flow cytometry as described in ref. 25 2.5 h after i.v. injection of nanoparticles. (We chose an early time point to allow measurement of cellular effects before cells in the periphery are replaced by bone marrow progenitors, and specifically included splenic monocytes because they are an important source of marginating monocytes that exchange with the circulating pool.) In the spleen, Qdot-NH_2-PEG causes a significant increase in the monocyte fraction (0.89 ± 0.08) compared with either Feridex IV or CLIO-NH_2 (0.43 ± 0.15, 0.48 ± 0.06; $P = 0.0030$ for ANOVA), both of which are comparable with control (buffer alone) (Fig. 6 *a* and *b*). Consistent with our *in vitro* clustering results, Feridex IV and CLIO-NH_2 cause similar effects on monocytes *in vivo* ($P > 0.05$), and Qdot-NH_2-PEG causes a distinct effect ($P < 0.01$ vs. either Feridex IV or CLIO-NH_2). The same trend is evident in peripheral blood, with a dramatically increased monocyte fraction induced by Qdot-NH_2-PEG (2.87 ± 1.92) compared with Feridex IV or CLIO-NH_2 (0.62 ± 0.56, 0.34 ± 0.03; $P = 0.069$ for ANOVA) (Fig. 6 *a* and *c*). None of the nanoparticles causes a significant increase in acute necrotic or apoptotic cell death at the concentrations tested, as assessed through propidium iodide uptake or annexin V binding (data not shown).

Discussion

This work suggests a generalizable and scalable method for the systematic characterization and comparison of novel nanomaterials. Here, we show that the incorporation of multiple assays and cell types leads to different correlations among nanoparticles (Figs. 2 and 5). We also show that hierarchical clustering of activity profiles places nanoparticles in functionally meaningful groupings, such as a cluster containing nanoparticles that are either FDA-approved, or are close analogs of nanoparticles that have completed phase III clinical trials (Fig. 3 *a* and *c*). Detailed structure–activity relationships result from the study of related nanomaterials, including instances where the activity profiles are dominated by either core composition (Fig. 4*a*) or surface modifications (Fig. 4*b*); the power of our approach to distinguish subtle alterations in composition is exemplified by the distinct activity profiles of nanoparticles differing only by diastereomeric peptide modifications (Fig. 4*b* and Fig. S3*b*).

To our knowledge, this is the largest evaluation of nanomaterials in the literature to date, involving data on 50 nanoparticles collected from ≈24,000 wells. The ability to evaluate nanomaterials in high-throughput is helpful given the vast number of possible compositions and enables detailed structure–activity relationships to emerge from the study of families of closely related materials, using multiple assays and cell types. Although we chose four assays and cell types for these proof-of-concept experiments, the optimal number and choice of assays and cell types for future applications remains to be determined. For instance, to investigate nanomaterials where the primary route of exposure was by inhalation, one might consider including bronchial or alveolar epithelial cells among the cell types studied. A wide variety of assays could also be contemplated, such as measures of DNA replication or in-plate Western blots assessing the phosphorylation state of specific proteins; as the cost of measuring genome-wide gene expression decreases, it may become feasible to systematically characterize nanomaterials based on gene expression. It is not yet clear whether different applications require unique assay and cell type choices or whether a certain repertoire would be sufficiently orthogonal for most applications; the analyses outlined here can guide the selection of a suite of assays and cell types that efficiently extracts informative data for any collection of nanomaterials to be tested.

We characterize nanomaterials based on their activity profile, which incorporates data from several cell-based assays and cell types; these profiles then become the unit of analysis as we group or classify nanoparticles according to their patterns of activity. This profile-based approach is fundamentally distinct from prior efforts to characterize nanomaterials *in vitro*. For instance, a profile-based analysis samples a much wider swath of biology and should be less sensitive to any peculiarities of a particular cell line or assay. Equally important, our analysis does not seek to directly extrapolate from an *in vitro* assay to an *in vivo* phenotype; previous attempts at such extrapolation have been problematic for several potential reasons (e.g., altered cellular phenotypes during tissue culture, or interactions of the nanoparticles with the culture media). Because our analysis compares biologic activity across nanoparticles (all of which are analyzed under uniform media and culture conditions), we can still draw conclusions as to similarities or differences among nanoparticles based upon our *in vitro* data.

Our emphasis on comparing across nanomaterials becomes increasingly useful as the number of well characterized reference nanomaterials (such as the FDA-approved Feridex IV) grows, because it allows the generation of testable hypotheses, namely, that nanomaterials that cluster close together with FDA-approved agents *in vitro* may also exhibit similar behavior *in vivo*. We tested this hypothesis by intravenously injecting three commonly used imaging nanomaterials of varying composition (Feridex IV, CLIO-NH_2, and Qdot-NH_2-PEG) (Table 1 and Table S1) and examining the monocyte fraction. These data show that similarities and differences in activity *in vitro* are borne out *in vivo*, at least for the nanoparticles tested. Although an increase in monocytes (such as that induced by Qdot-NH_2-PEG) has been associated with toxic exposures (22, 23), further studies are needed to clarify if the changes in monocyte level after Qdot-NH_2-PEG exposure correlate with other immune or adverse phenotypes.

An intriguing question raised by our data are whether a profile-based approach could provide an *in vitro* filter to help identify promising compounds for *in vivo* testing. More specifically, could one identify novel nanomaterials that are likely to have favorable *in vivo* safety based on *in vitro* activity profiles that are similar to an FDA-approved material? Answering this question requires empirically optimizing *in vitro* assays and cell types and analytic methods, but the overall approach outlined in this report could serve as a template for these efforts. As the development of nanomaterials for a wide range of applications continues to accelerate, this approach could provide a powerful tool to guide the development and toxicity evaluation of future nanomaterials.

Methods

Cell Types. Endothelial cells (human aorta) and vascular smooth muscle cells (human coronary artery) were purchased from Cambrex and were grown in

EBM-2 and SmBC media (Cambrex), respectively. Hepatocytes (human HepG2 cells) were grown in CellGro MEM plus 10% FBS, 2 mM sodium pyruvate and 1% penicillin/streptomycin (pen/strep). The murine RAW 264.7 leukemic monocyte/macrophage cell line was grown in CellGro DMEM plus 10% FBS, 2 mM L-glutamine and 1% pen/strep.

Cell-Based Assays. Cells were plated into 384-well plates and incubated overnight; nanoparticles were incubated for 4 h in a total volume of 30 μl. [Pilot experiments showed that a 4-h incubation was sufficient to allow differences in nanoparticles to become apparent without causing nondiscriminate cell death at the highest doses tested (data not shown). Thus, the 4-h time point was chosen to elucidate similarities and differences among nanoparticles and not as an attempt to model some physiologic time of exposure.] Nanoparticle final concentrations were 0.01, 0.03, 0.1, and 0.3 mg/ml Fe for iron-based nanoparticles to encompass intravascular concentrations achieved during human studies (e.g., a widely cited study injected an intravascular nanoparticle imaging agent (Combidex) at 2.6 mg/kg Fe; assuming a weight of 70 kg and an intravascular volume of 5 l, this corresponds to an intravascular dose of ≈0.03 mg/ml Fe (26). Quantum dots were tested at final concentrations of 3, 10, 30, or 100 nM, which encompass a range from ≈1–50× doses used for *in vitro*- (27) or *in vivo*- (28) labeling experiments. The JC1 (mitochondrial membrane potential) (Molecular Probes), CellTiter-Glo (ATP content; Promega), Apo-ONE Caspase-3/7 (apoptosis; Promega), and C12-resazurin (reducing equivalents; Molecular Probes) assays largely followed manufacturer instructions, and nanoparticles were excluded from analysis if their intrinsic fluorescence interfered with an assay (details are in *SI Methods*).

Coefficients of variation {%CV = [(SD)/$\sqrt{n}$]/mean × 100, where $n = 4$ replicates per condition} for the four assays were: JC1 9%, CTG 5%, Apo-ONE 6%, and C12-resazurin 10%, which are well within assay guidelines published by the National Institutes of Health Chemical Genomics Center (29). Each experimental condition was analyzed in quadruplicate and compared with 172 control wells (containing PBS) on the same plate. *Z* scores for each nanoparticle condition (Z_{NP}) were calculated as: $Z_{NP} = (\mu_{NP} - \mu_{PBS})/\sigma_{PBS}$, where μ and σ are the mean and standard deviation, respectively.

***In Vivo* Monocyte Analysis.** Protocols were approved by the animal care and use committee of the Massachusetts General Hospital and Center for Molecular Imaging Research. BALB/c mice received intraorbital i.v. injections of agents in 100 μl of PBS: 20 mg/kg CLIO-NH2; 160 pmol of QDot-NH2-PEG, 20 mg/kg Feridex, or none (PBS). Two hours and 30 min later, white blood cells were purified from peripheral blood and spleen as described in ref. 25. Single cell suspensions were labeled with appropriate markers to identify monocytes [e.g., CD11b^{hi} (CD90/B220/CD49b/NK1.1/Ly-6G)^{lo} cells] by flow cytometry (25). Cells were analyzed for Annexin V binding and propidium iodide uptake (30). Mean monocyte levels were measured in three mice per agent and compared by using one-way ANOVA and the Bonferroni multiple comparisons test for posttest comparisons.

Nanoparticle Synthesis and Characterization. Table S1 lists the coating, surface modification, size, relaxivities, zeta potential, and source/citation for the nanoparticles tested. Nanoparticle size and zeta potential were measured by using a Zetasizer 1000 (Malvern Instruments); relaxivities were determined by using a Bruker Minispec MQ20 NMR.

Clustering Analysis. Hierarchial and consensus clustering and class prediction analyses used the appropriate modules in GenePattern 3.1 (31). For hierarchical clustering, pairwise average linkage clustering was used; nanoparticles were clustered by using Pearson correlation and assay conditions were clustered by using Euclidean distance; other analyses used default parameters. Details are in *SI Methods*.

Correlations Between Data Subsets. For each data subset, we calculated the pairwise Pearson correlation between all possible combinations of the 50 nanoparticles, based on their *Z* score profiles across combinations of dose, cell type, and assay. This generates 15 (50 × 50) matrices (whose elements are the pairwise Pearson correlations), one for each data subset (1 combination of four assays, four combinations of three assays, six combinations of two assays, and four ways to use one assay). We then calculated the pairwise Pearson correlations between these fifteen 50 × 50 matrices, resulting in a single 15 × 15 matrix in which each element reflects the correlation between two data subsets. Finally, we calculated the average correlation with the complete (four-assay) dataset for all datasets incorporating one, two, three, or four assays; these were compared using a one-way ANOVA; the correlation for subsets using three, two, or one assays was compared with 1 (the correlation of the complete dataset with itself), using a one-sided, one-sample *t* test. An analogous analysis was performed for data subsets that use varying numbers of cell types.

ACKNOWLEDGMENTS. This work was supported by the National Institutes of Health National Heart, Lung, and Blood Institute Grant U01HL080731 (to S.Y.S. and R.W.), National Cancer Institute Grant P50CA086355 (to R.W.), National Cancer Institute Grant U54CA119349 (to R.W.), and National Heart, Lung, and Blood Institute Grant K08HL077186 (to S.Y.S.), the Broad Institute of Harvard and MIT (to S.Y.S., R.W., and S.L.S.), and the de Gunzburg Family Foundation at Massachusetts General Hospital (S.Y.S.). This project has been funded in whole or in part with Federal funds from the National Cancer Institute's Initiative for Chemical Genetics, National Institutes of Health, under Contract no. N01-CO-12400 and has been performed with the assistance of the Chemical Biology Platform of the Board Institute of Harvard and MIT.

1. Stern ST, McNeil SE (2008) Nanotechnology safety concerns revisited. *Toxicol Sci* 101:4–21.
2. Lam CW, James JT, McCluskey R, Hunter RL (2004) Pulmonary toxicity of single-wall carbon nanotubes in mice 7 and 90 days after intratracheal instillation. *Toxicol Sci* 77:126–134.
3. Warheit DB, *et al.* (2004) Comparative pulmonary toxicity assessment of single-wall carbon nanotubes in rats. *Toxicol Sci* 77:117–125.
4. Maynard AD, *et al.* (2006) Safe handling of nanotechnology. *Nature* 444:267–269.
5. Durr E, *et al.* (2004) Direct proteomic mapping of the lung microvascular endothelial cell surface *in vivo* and in cell culture. *Nat Biotechnol* 22:985–992.
6. Worle-Knirsch JM, Pulskamp K, Krug HF (2006) Oops they did it again! Carbon nanotubes hoax scientists in viability assays. *Nano Lett* 6:1261–1268.
7. Golub TR, *et al.* (1999) Molecular classification of cancer: Class discovery and class prediction by gene expression monitoring. *Science* 286:531–537.
8. Scherf U, *et al.* (2000) A gene expression database for the molecular pharmacology of cancer. *Nat Genet* 24:236–244.
9. Shi LM, *et al.* (2000) Mining and visualizing large anticancer drug discovery databases. *J Chem Inf Comput Sci* 40:367–379.
10. Sosnovik DE, Weissleder R (2007) Emerging concepts in molecular MRI. *Curr Opin Biotechnol* 18:4–10.
11. Wunderbaldinger P, Josephson L, Weissleder R (2002) Cross-linked iron oxides (CLIO): A new platform for the development of targeted MR contrast agents. *Acad Radiol* 9 (Suppl 2):S304–S306.
12. Shen T, Weissleder R, Papisov M, Bogdanov AJ, Brady TJ (1993) Monocrystalline iron oxide nanocompounds (MION): Physicochemical properties. *Magn Reson Med* 29:599–604.
13. Michalet X, *et al.* (2005) Quantum dots for live cells, *in vivo* imaging, and diagnostics. *Science* 307:538–544.
14. Metz S, *et al.* (2004) Capacity of human monocytes to phagocytose approved iron oxide MR contrast agents *in vitro*. *Eur Radiol* 14:1851–1858.
15. Long TC, *et al.* (2007) Nanosize titanium dioxide stimulates reactive oxygen species in brain microglia and damages neurons *in vitro*. *Environ Health Perspect* 115:1631–1637.
16. Davoren M, *et al.* (2007) *In vitro* toxicity evaluation of single walled carbon nanotubes on human A549 lung cells. *Toxicol In Vitro* 21:438–448.
17. Choi AO, Cho SJ, Desbarats J, Lovric J, Maysinger D (2007) Quantum dot-induced cell death involves Fas upregulation and lipid peroxidation in human neuroblastoma cells. *J Nanobiotechnology* 5:1.
18. Monti S, Tamayo P, Mesirov JP, Golub T (2003) Consensus Clustering: A resampling-based method for class discovery and visualization of gene expression microarray data. *Machine Learn J* 52:91–118.
19. Pittet MJ, Swirski FK, Reynolds F, Josephson L, Weissleder R (2006) Labeling of immune cells for *in vivo* imaging using magnetofluorescent nanoparticles. *Nat Protoc* 1:73–79.
20. Weissleder R, *et al.* (1989) Superparamagnetic iron oxide: Pharmacokinetics and toxicity. *AJR Am J Roentgenol* 152:167–173.
21. Ros PR, *et al.* (1995) Hepatic MR imaging with ferumoxides: A multicenter clinical trial of the safety and efficacy in the detection of focal hepatic lesions. *Radiology* 196:481–488.
22. Filep JG, Fournier A, Foldes-Filep E (1995) Effects of the ETA/ETB receptor antagonist, bosentan on endothelin-1-induced myocardial ischaemia and oedema in the rat. *Br J Pharmacol* 116:1745–1750.
23. Stephen M, Woo J, Hasan NU, Whiting PH, Thomson AW (1989) Immunosuppressive activity, lymphocyte subset analysis, and acute toxicity of FK-506 in the rat. A comparative and combination study with cyclosporine. *Transplantation* 47:60–65.
24. Dobrovolskaia MA, McNeil SE (2007) Immunological properties of engineered nanomaterials. *Nat Nanotech* 2:469–478.
25. Nahrendorf M, *et al.* (2007) The healing myocardium sequentially mobilizes two monocyte subsets with divergent and complementary functions. *J Exp Med* 204:3037–3047.
26. Harisinghani MG, *et al.* (2003) Noninvasive detection of clinically occult lymph-node metastases in prostate cancer. *N Engl J Med* 348:2491–2499.
27. Howarth M, Takao K, Hayashi Y, Ting AY (2005) Targeting quantum dots to surface proteins in living cells with biotin ligase. *Proc Natl Acad Sci USA* 102:7583–7588.
28. Kobayashi H, *et al.* (2007) Simultaneous multicolor imaging of five different lymphatic basins using quantum dots. *Nano Lett* 7:1711–1716.
29. Eli Lilly & Co., National Institutes of Health Chemical Genomics Center (2005) Assay Guidance Manual Version 4.1.
30. Swirski FK, *et al.* (2007) Ly-6Chi monocytes dominate hypercholesterolemia-associated monocytosis and give rise to macrophages in atheromata. *J Clin Invest* 117:195–205.
31. Reich M, *et al.* (2006) GenePattern 2.0. *Nat Genet* 38(5):500–501.